The Astrophysical Journal, 803:106 (14pp), 2015 April 20 doi:10.1088/0004-637X/803/2/106

X-RAY SPECTROSCOPY OF POTENTIAL SMALL MAGELLANIC CLOUD TYPE Ia SUPERNOVA REMNANTS AND THEIR ENVIRONMENTS

Q. Roper[1], R. L. McEntaffer[1], C. DeRoo[1], M. Filipovic[2], G. F. Wong[2], and E. J. Crawford[2]
[1] Department of Physics and Astronomy, University of Iowa, Van Allen Hall, Iowa City, IA 52242, USA; quentin-roper@uiowa.edu
[2] University of Western Sydney, Locked Bag 1797, Penrith South DC, NSW 1797, Australia
Received 2014 March 3; accepted 2015 February 12; published 2015 April 22

ABSTRACT

We examine three supernova remnants in the SMC, IKT 5 (supernova remnant (SNR) 0047-73.5), IKT 25 (SNR 0104-72.3), and DEM S 128 (SNR 0103-72.4), which are designated as Type Ia in the literature due to their spectra and morphology. This is troublesome because of their asymmetry, a trait not usually associated with young Type Ia remnants. We present *Chandra X-ray Observatory* data on these three remnants and perform a maximum likelihood analysis on their spectra. We find that the X-ray emission is dominated by interactions with the interstellar medium. In spite of this, we find a significant Fe overabundance in all three remnants. Through examination of radio, optical, and infrared data, we conclude that these three remnants are likely not Type Ia SNRs. We detect potential point sources that may be members of the progenitor systems of both DEM S 128 and IKT 5, which could suggest these could be Fe-rich core-collapse remnants.

Key words: ISM: individual objects (IKT 25, IKT 5, DEM S 128) – ISM: supernova remnants – methods: statistical

1. INTRODUCTION

Although much work has been produced in the *Chandra* and *XMM-Newton* era on the supernova remnant (SNR) population of the SMC, there is a subset of these remnants that are relatively understudied in the X-ray regime. This is at least in part due to their relative dimness in X-rays. van der Heyden et al. (2004) performed a detailed study of 13 SNRs using *XMM-Newton* and typed these objects based on morphology and spectral properties. In particular, they grouped three remnants, IKT 25, DEM S 128, and IKT 5 as probable Type Ia candidates, the result of thermonuclear detonation of a white dwarf. Their spectra are dominated by a single broad peak around 1 keV, with little else in the way of line emission. This broad peak could be associated with Fe-L shell emission arising from shock-heated ejecta, thus leading to the Type Ia designations. In addition, they are markedly different from other SMC SNRs in morphology, being very asymmetric in the soft X-ray band, as opposed to other, more symmetric core-collapse (CC) SNRs. SNR 0102-72.3 is a well-studied CC remnant (Flanagan et al. 2004), yet is highly symmetric both circularly and bilaterally. Other CC remnants in van der Heyden et al. (2004) also show high degrees of symmetry, such as IKT 6 (SNR 0049-73.6) and IKT 23 (SNR 0103-72.6).

In recent years, there has been a number of studies that attempt to characterize SNRs by their morphology. Previous studies have shown a link between soft X-ray morphology and progenitor type. Lopez et al. (2011) performed a survey of the young line-dominated LMC and galactic SNRs by analyzing the two-dimensional multipole moments of counts in the soft X-ray regime. When examining the quadrupole versus octupole moments, this population of SNRs was divided into two groups, with Type Ia SNRs having lower quadrupole and octupole moments, thus being more symmetrical in shape, both circularly and bilaterally, than their CC cousins. However, if the typing of SMC SNRs in van der Heyden et al. (2004) is correct, the Lopez et al. (2011) trend appears to be in stark contradiction to the SMC remnants. The previously mentioned SMC CC remnants appear to be relatively symmetric, both circularly and bilaterally. On the other hand, the three previously mentioned Type Ia candidates are highly asymmetric, thus displaying a morphological dichotomy in the SMC that is opposite to that found in the LMC or Milky Way. We present here a study aimed at providing further clarity to this apparent contradiction through spectral and spatial analysis of *Chandra* data for these Type Ia candidates, IKT 25, DEM S 128, and IKT 5. Detailed spectral analysis will either provide new insight into these objects and challenge their classification or confirm the *XMM-Newton* study, thus solidifying the curious difference between the SMC and its closest neighbors.

IKT 25 is the brightest of these three remnants in the X-ray band. Hughes & Smith (1994) presented *ROSAT* observations alongside CTIO Hα images and concluded that an unresolved point source in the X-ray has an Hα counterpart, thus suggesting a Be X-ray star association within the remnant. Lee et al. (2011) have performed a recent study utilizing the high spatial resolution of *Chandra* and find that this putative Be star is actually an extended knot of plasma. They find evidence of nonequilibrium plasma conditions and a marginal detection of Fe overabundance. Because it is seated within a complex environment, they conclude that IKT 25 is an example of a "prompt" Type Ia, whose progenitor system evolves to the supernova stage faster than typical (Borkowski et al. 2006).

DEM S 128 was initially identified through a survey of Hα emission nebulae (Davies et al. 1976). Inoue et al. (1983) reported the first X-ray observation of this remnant and detected an extended X-ray counterpart nearby to this Hα region, naming it IKT 24. Filipović et al. (2000) reported a continuum 843 MHz ATCA observation of this remnant and found significant radio emission. They compute radio spectral indices for sources coincident with the remnant and nearby X-ray sources RX J0105.5-7213, RX J0105.6-7211, and RX J0104.9-7210. They classify RX 0105.5-7213 as a background active galactic nucleus but are unable to classify the other two sources. They calculate a radio spectral index for DEM S 128 of $\alpha = -0.65$ suggesting an evolved SNR shock. Following this work, Filipović et al. (2005) observe the northern section

of the remnant at 2.37 GHz and show that the emission is constrained to a few bright spots that are uncorrelated with previous X-ray data, suggesting a complicated environment. Finally, Payne et al. (2007) report an S II/Hα ratio of DEM S 128 of 0.6, which is also consistent with the shell of an evolved remnant.

There is a paucity of observations on IKT 5. The first X-ray detection of IKT 5 was part of a large SMC survey by the *Einstein Observatory* (Inoue et al. 1983). In the optical, Payne et al. (2007) utilized long-slit spectroscopy to analyze IKT 5 along with other remnants in the SMC and found it to have a very high S II 6716 Å/ 673 Å line ratio. They also present a combined Hα and 843 MHz continuum image. Laycock et al. (2010) searched for X-ray binaries (XRB) in the SMC in the neighborhood of this remnant. They report finding an X-ray point source in the interior, labeled CXOU J004824-731918, but they conclude that due to the lack of a bright optical counterpart, this point source is likely not an X-ray binary. This leaves the possibility of another type of compact object.

The goal of our investigation is to conglomerate data at multiple wavelengths in order to better understand these potential Type Ia SNRs. Are they truly Type Ia remnants, with characteristic overabundance of Fe, or is there some other explanation of their X-ray 1 keV spectral feature? To what extent can their multiwavelength morphologies aid in determining their respective progenitor systems, if at all? What role do their environments play in determining their morphology? Does the environment of the remnant dominate morphology, or does the ejecta? Our goal is to provide insight to these questions with regard to IKT 5, IKT 25, and DEM S 128 and ultimately shed light on the SNR morphology dichotomy.

2. OBSERVATIONS

The observations of IKT 25 total 112 ks over two observations of on-axis time on the ACIS S-3 chip (observation IDs 9100 and 9810). In these same observations, another of these remnants, DEM S 128, was serendipitously detected on the ACIS S-2 chip (~6.′5 off-axis). Due to its front-illuminated nature, ACIS S-2 is less sensitive to the soft X-rays that dominate the emission of all three of these remnants. IKT 5 was also serendipitously observed as part of a deep-field observation searching for XRB in the SMC. As such, IKT 5 appears off-axis (~7.′5) for a total of 98 ks over three observations on the ACIS I-1 chip (observation IDs 7156, 8179, and 8481), which is also front-illuminated.

In order to analyze and extract images and spectra from these observations, we use the *Chandra* Interactive Analysis of Observations (CIAO) software package (Fruscione et al. 2006) version 4.4 with the Calibration Database (CALDB) version 4.4.8. All the data sets are reprocessed using the CIAO script *chandra_repro* in order to ensure the most modern and relevant calibrations were applied to the data sets. The observations of each remnant are merged using the *dmmerge* tool. The X-ray images were binned to the natural *Chandra* ACIS instrument resolution. The X-ray data were adaptively smoothed using the CIAO tool *dmimgadapt* using a Gaussian kernel. The X-ray images, adaptively smoothed, can be seen at the top of Figures 1–3.

To augment our analysis of these X-ray data, we examine the three remnants at different wavelengths. We analyze 20 cm data from the ATCA, which were reduced using MIRIAD (Sault et al. 1995). The infrared and optical data we present were taken with the *Spitzer Space Telescope*'s IRAC instrument, obtained through the *Spitzer* Heritage Archive, and optical data from the Magellanic Cloud Emission Line Survey (MCELS) in continuum-subtracted Hα, [S II], and [O III] bands. These particular wavebands have been included in order to qualitatively characterize the environments in which these SNRs are located.

3. X-RAY SPECTRAL ANALYSIS

Extraction regions for spectral analysis are determined through inspection of the X-ray images. The CIAO script *specextract* is used to extract spectra from regions, as well as produce the response matrices. The CIAO script *combine_spectra* is subsequently used to combine all the spectra from a given region into a single spectrum for analysis. For each remnant, there may be X-ray sources that are discrete and distinctive from the shocked plasma. In order for the X-ray plasma to be uncontaminated by these sources, we perform a point-source extraction to detect and exclude their contribution. To find these potential offenders, we used the CIAO tool *wavdetect* with wavelet transformation scales of 0.″5, 1″, 2″, and 4″. The output provides region files that encompass the 3σ extent of each source, where σ is the uncertainty in the point-spread function (PSF). To utilize this tool, we produced the expected off-axis PSF of *Chandra* using the *mkpsfmap* CIAO tool. After determination of point-source contributions, we chose extraction regions for each remnant based on suggestions from the apparent X-ray morphology. First, the X-ray emission of IKT 25 exhibits an apparent bipolar morphology roughly NW–SE, suggesting an analysis of regions along the axis of emission. This results in two extraction regions in the north (labeled A and B) and two in the south (labeled C and D), in addition to a region (the "Wisp") that includes a faint arc of emission evident in the east. Second, due to the low surface brightness of DEM S 128, we only use one X-ray extraction region for the entire remnant. Finally, the X-ray morphology of IKT 5 suggests two extraction regions: one in the north (northern) that corresponds to the more circular, diffuse emission surrounding the supposed point source, and one in the south (southern) that contains the wispy, more tenuous emission. The bottom of Figures 1–3 displays the X-ray data, with extraction regions overlaid.

A variety of thermal and nonthermal models are considered to find the best fit to these spectra using the *CIAO* fitting package, *Sherpa* (Freeman et al. 2001). We might expect some or all of these remnants to be in collisional ionization equilibrium (CIE) if they are older or in areas of enhanced density. In this case the plasma will be well described by the *xsvapec* model with the most up-to-date atomic processes in AtomDB 2.0.2 (Foster et al. 2012). If the plasma composing the SNR is younger or in a lower density regime, then the nonequilibrium model for singly shocked plasma, *xsvnei*, should accurately describe the spectra. The *xsvnei* model is used with an augmented line list from Kazik Borkowski that includes additional inner shell atomic processes (for a more complete explanation, see Badenes et al. 2006). A plane-parallel shock model, *xsvpshock,* is similar to *xsvnei*, but with a range of ionization timescales, which we might expect to see in regions where there are significant density gradients or complex ISM morphology. We fit these thermal models to the extracted spectra and also investigate contributions from nonthermal plasmas through the addition of a power-law component, using the *xspowerlaw* model. Elemental

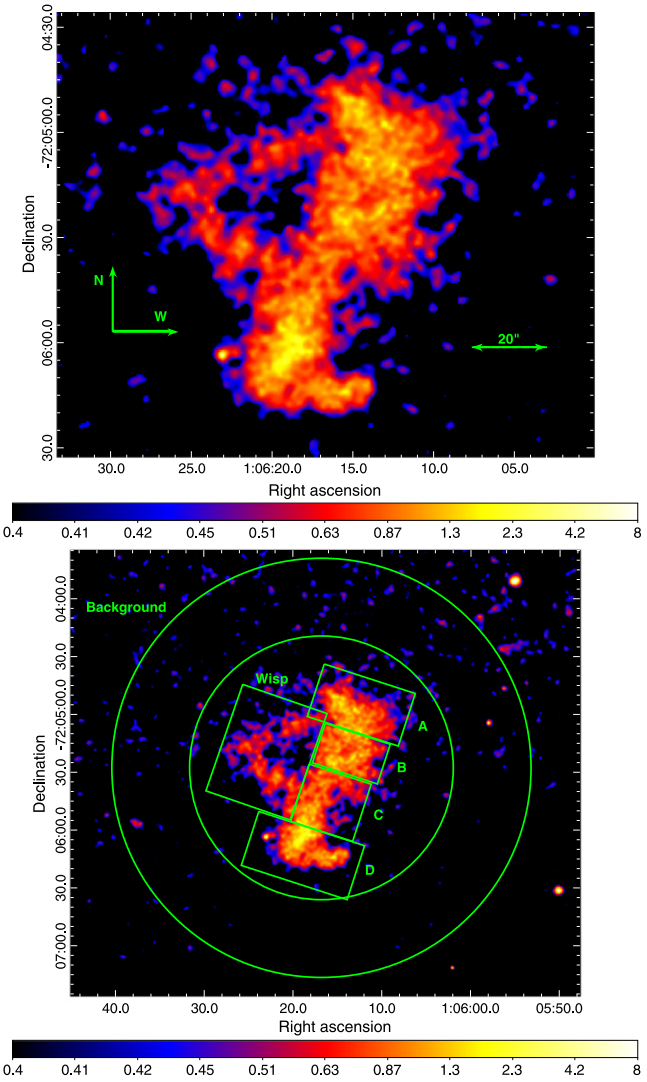

Figure 1. X-ray data of IKT 25. Broadband ACIS images (0.5–8 keV) of IKT 25, binned to the ACIS instrumental resolution (0.″5 per pixel) and adaptively smoothed using the *dmimgadapt* CIAO tool, with a kernel of 16 counts over scales from 0.5 to 16 pixels (top) and with spectral extraction regions overlaid (bottom). The color-bar scales are in counts/pixel.

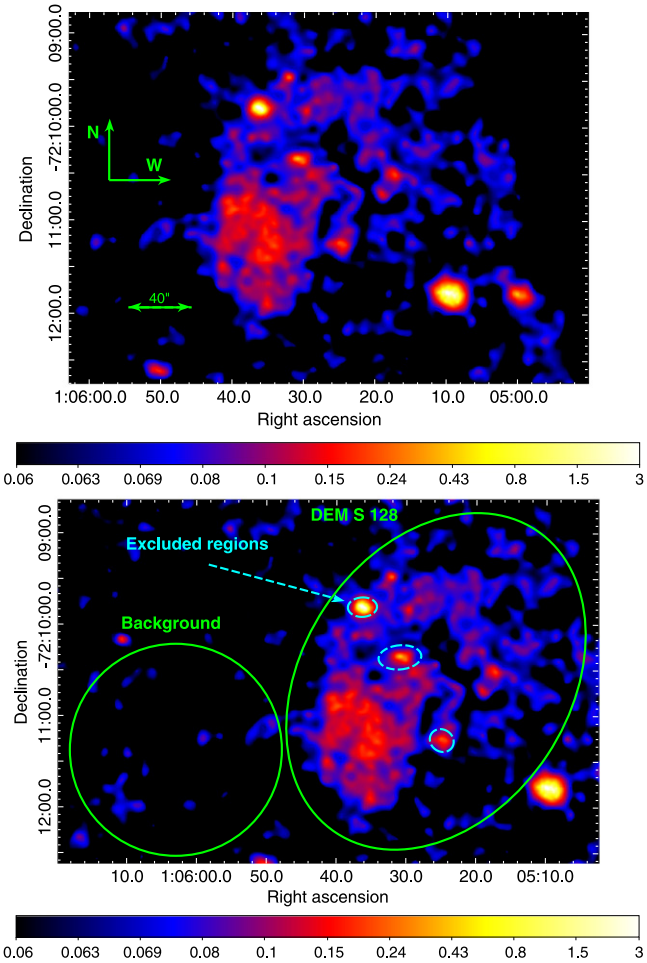

Figure 2. (a) X-ray data of DEM S 128. Broadband ACIS images (0.5–8 keV) of DEM S 128, binned to the ACIS instrumental resolution and adaptively smoothed, as in Figure 1. (b) X-ray image of DEM S 128 with spectral extraction regions overlaid. The color-bar scales of both images are in counts/pixel.

abundances are allowed to vary if statistically significant and are set to those of the SMC ISM per Russell & Dopita (1992): He 0.83, C 0.13, N 0.05, O 0.15, Ne 0.19, Mg 0.24, Al 0.80 (for *xsvapec* only), Si 0.28, S 0.21, Ar 0.16, Ca 0.21, Fe 0.20, and Ni 0.40, where a value of 1.0 signifies solar abundances. Since the majority of our X-ray emission exists between 0.7 and 1.0 keV, we pay particular attention to Fe-L shell emission lines and lines from Ne IX and Ne X in our fits, which are overabundant in the VDH04 fits.

The source spectral models are convolved through two separate absorption columns: one representing galactic absorption, *xstbabs*, with absorbers at galactic abundances and one representing absorption within the SMC, with SMC abundances, *xstbvarabs*. The galactic component is frozen at $N_H = 0.046 \times 10^{22}$ cm^{-2} for IKT 25 and DEM S 128 and at $N_H = 0.052 \times 10^{22}$ cm^{-2} for IKT 5 (Dickey & Lockman 1990), whereas the SMC component's hydrogen column density is allowed to vary. We choose *xstbabs* as a modern and complete absorption model, with abundances derived from Wilms et al. (2000) and photoionization cross-sections derived from Verner et al. (1996).

When performing spectral fitting, we use the Cash statistic (Cash 1979), which is a Poisson-likelihood statistic, as opposed to the χ^2 statistic. The latter assumes a Gaussian likelihood, whereas the Cash statistic better represents the distribution of counts per bin in the low-counts regime and is more appropriate for this investigation. In order to evaluate goodness-of-fit, we generate a distribution of best-fit statistics we expect, given the best-fit model and degrees of freedom. We construct this distribution by evaluating the best-fit model onto the spectral bins, adding in a Poisson noise component and evaluating the Cash statistic when the model is reapplied to the synthesized spectra. Repeating this process many times, we can construct a distribution of Cash statistics we might expect, given the model and degrees of freedom. If the statistic we derive from fitting the spectrum extracted from the observation is extreme compared to the distribution of statistics generated from the synthesized spectra, we rule out the fit. In our best-fit tables, Tables 1–3, we state the probability of finding a best-fit statistic lower than the one obtained in our fit, which we label 1 − (P-value).

In order to determine the statistical significance of additional model components, a variation of the likelihood ratio test

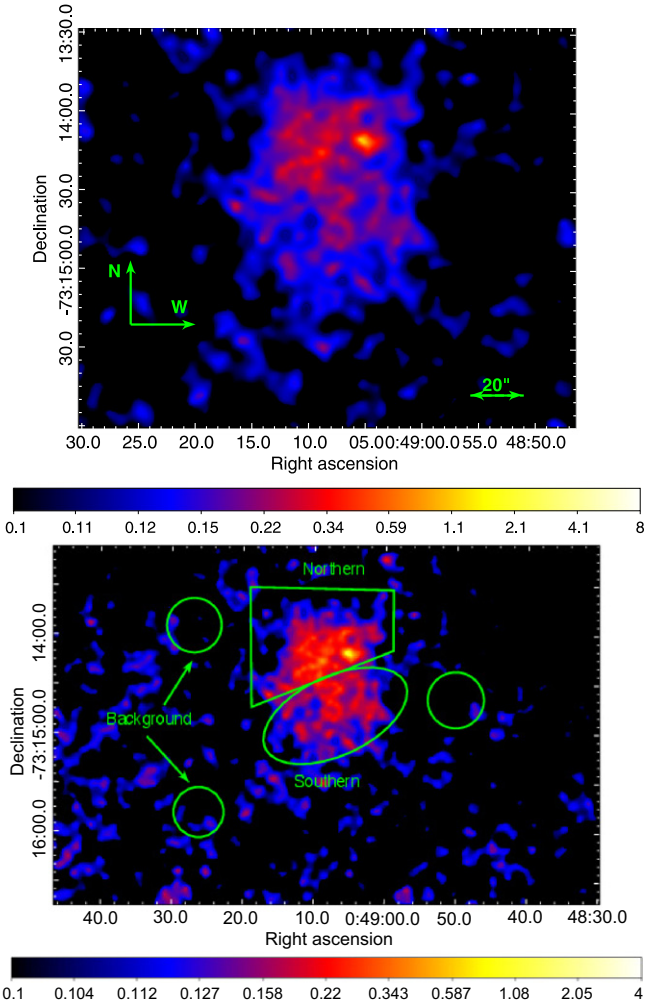

Figure 3. (a) X-ray image of IKT 5. Broadband ACIS images (0.5–8 keV) of IKT 5, binned to the ACIS instrumental resolution and adaptively smoothed, as in Figure 1. (b) X-ray image of IKT 5 with spectral extraction regions overlaid (bottom). The color-bar scales are in counts/pixel.

(LRT) is employed. As noted by Protassov et al. (2002), the LRT is not usable in the case when the simpler model is on the boundary of the parameter space of the more complicated model, as is the case when testing for an additional thermal model. This is because the null distribution used to judge the likelihood ratio is uncalibrated and, in general, analytically unknown. In order to solve this problem, we construct the null distribution of the LRT numerically by evaluating the likelihood ratio on synthetic spectra produced by adding a Poisson noise component to the best-fit simpler model. Due to computational limitations, we perform this 400 times for each spectrum. If the likelihood ratio is sufficiently high when compared to the constructed null distribution, we can be confident that the more complicated model is a better description of the spectrum, rather than an artificial improvement due to the more complicated model having more free parameters. We adopt a P-value of 0.1 to be the maximum for which we consider the more complicated model "better", i.e., the fit improvement has to be greater than the 90th percentile of the constructed null distribution to be considered a significant improvement over the simpler model. In this way, we numerically construct the LRT null distribution and restore its usefulness in distinguishing between a spectrum produced by one thermal component or by two thermal components. This method is similar to, but not identical to, the parametric bootstrapping described in Section 5.2 of Protassov et al. (2002).

4. RESULTS

4.1. IKT 25

For IKT 25, the best-fit models and their best-fit parameters are shown in Table 1. The spectra we obtained, with best-fit model overlaid, can be seen in Figures 4 and 5. Regions A, B, and D are best-fit with a CIE plasma model with temperature of ~1.0 keV. Region C is best fit with a two-temperature model with a CIE component at kT ~0.6 keV and an NEI component at kT ~ 1.0 keV. When we fit this region with a one-temperature CIE plasma model, it resulted in a temperature of around 1.0 keV, similar to the other three regions. Adding the NEI component decreased our statistic from 202/195 to 188/192, which was significant, with a P-value of 0.0025 (See Figure 8). In all regions we require an enhanced Fe abundance in order to fit the spectra, and in all regions the significance of the Fe overabundance was >5σ. With the Wisp, we found the best-fit model to be a two-temperature model as in Region C, with one important difference: we found a 5σ enhanced silicon abundance in addition to enhanced iron abundance. The improvement to the fit when compared to a single-temperature CIE model is significant, with a P-value of 0.0026 (Figure 8). The absorbing column density N_H varies greatly across the remnant, with Regions A, B, and D having a relatively small absorbing column density, at $<6 \times 10^{21}$ cm^{-2}. Regions C and the Wisp have a much larger absorbing column density at $\sim 1.5 \times 10^{22}$ cm^{-2}, and this higher absorbing column density is retained if only one thermal component is assumed.

4.2. DEM S 128

The best-fit model of the X-ray spectrum of DEM S 128 is given in Table 2 and is overlaid onto the extracted spectrum in Figure 6. With only one region extracted from DEM S 128, it is impossible to say anything about the spatial distribution of material in the SNR. However, in comparison to IKT 25, the absorbing column density is consistent with Regions A, B, and D at $\sim 3.5 \times 10^{21}$ cm^{-2}. Again, Fe was necessary to vary in the fit. As in IKT 25, the Fe abundance was enhanced at ~1.0 solar and was very significant at ~7 σ. All other elements were set to SMC abundance. Only one CIE thermal component was required, but the temperature was somewhat cooler than in IKT 25, at 0.65 keV.

4.3. IKT 5

The extraction regions for IKT 5 were chosen because the X-ray morphology suggests confinement in the north and extension toward the south. The best fits of the X-ray spectra obtained from the northern and southern regions can be found in Figure 7 and Table 3. As in IKT 25 and DEM S 128, we find an Fe overabundance in both the northern and southern regions of the remnant. The northern region has a ~6σ significant overabundance at 0.8 solar. The southern region has a higher Fe abundance at twice solar, but whose overabundance is much lower significance, at only ~2.5 σ. The northern region is well fit by a 0.94 keV equilibrium plasma. The southern region contains a lower-temperature equilibrium plasma at 0.56 keV

Table 1
Best-Fit Parameters for IKT 25 by Extraction Region

Region	Best-Fit Model	cstat/dof	1 - (P-value)	$N_{H,\mathrm{SMC}}$ (10^{22} cm^{-2})	kT_{vapec} (keV)	A_{Fe}	$\mathrm{norm}_{\mathrm{vapec}}$ (10^{-5} A)[a]	kT_{nei} (keV)	τ_{nei} (10^{11} cm^{-3} s)	$\mathrm{norm}_{\mathrm{nei}}$ (10^{-5} A)	A_{Si} Percentile	F-test P-value
A	$\mathrm{tbabs_{gal}} \times \mathrm{tbvarabs_{SMC}} \times$ vapec	202/195	75.0%	$0.58^{+0.15}_{-0.10}$	$0.95^{+0.02}_{-0.02}$	$1.2^{+0.2}_{-0.2}$	$6.1^{+0.7}_{-0.7}$	...	...	...	...	...
B	$\mathrm{tbabs_{gal}} \times \mathrm{tbvarabs_{SMC}} \times$ vapec	204/195	24.4%	$0.32^{+0.08}_{-0.08}$	$0.92^{+0.02}_{-0.03}$	$0.8^{+0.2}_{-0.1}$	$6.2^{+0.5}_{-1.0}$	...	...	...	...	...
C	$\mathrm{tbabs_{gal}} \times \mathrm{tbvarabs_{SMC}} \times$ (vapec + vnei)	188/192	10.6%	$1.4^{+0.6}_{-0.4}$	$0.68^{+0.04}_{-0.04}$	$0.7^{+0.2}_{-0.1}$	$1.2^{+0.2}_{-0.2}$	$0.98^{+0.05}_{-0.05}$	$2.8^{+0.2}_{-0.2}$	$1.4^{+0.2}_{-0.8}$	0.0026	
D	$\mathrm{tbabs_{gal}} \times \mathrm{tbvarabs_{SMC}} \times$ vapec	189/195	86.8%	$0.27^{+0.08}_{-0.07}$	$1.03^{+0.01}_{-0.02}$	$0.8^{+0.1}_{-0.1}$	$8.9^{+0.4}_{-0.7}$	...	...	...	...	...
Wisp	$\mathrm{tbabs_{gal}} \times \mathrm{tbvarabs_{SMC}} \times$ (vapec + vnei)	219/191	89.0%	$1.3^{+1.3}_{-0.3}$	$0.58^{+0.04}_{-0.04}$	$0.7^{+0.2}_{-0.1}$	$1.7^{+0.5}_{-0.4}$	$0.9^{+0.2}_{-0.1}$	>2.0	$0.9^{+0.4}_{-0.4}$	$1.3^{+0.3}_{-0.2}$	0.0025

Note. Spectral-fitting results by region listed in Figure 1. The remnant and regions are listed in the first two columns, with the next column indicating the best-fit model. Errors shown are analogous to 1σ. Abundances are shown relative to solar, with solar values equal to 1.

[a] Normalization parameter, where $A = [10^{-14}/(4\pi D^2)] \int n_e n_H dV$, D is the distance to the SMC, and the integral is the emission measure.

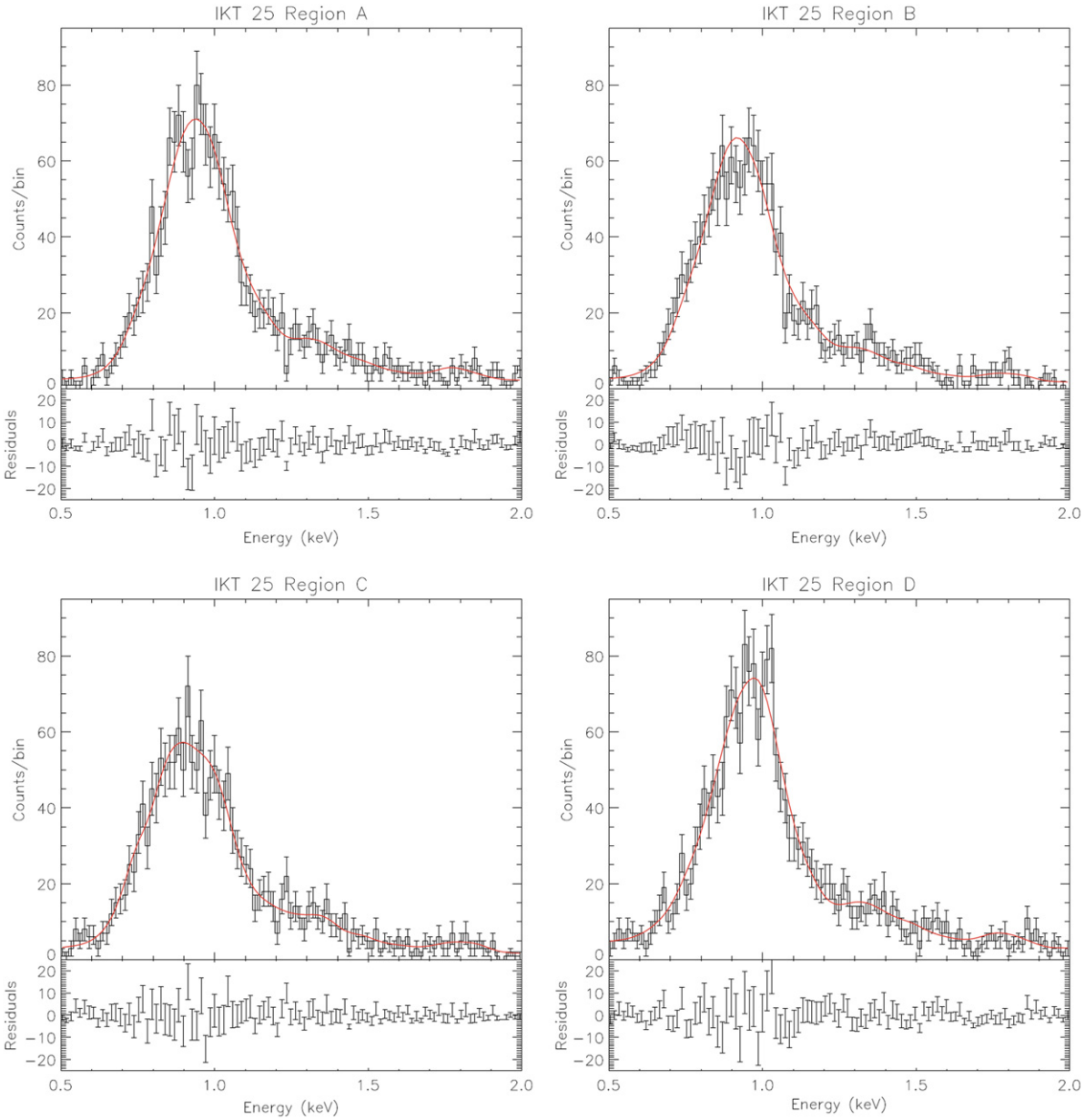

Figure 4. X-ray spectra extracted from IKT 25 from Regions A, B, C, and D in Figure 1 in black with best-fit models corresponding to the best-fit model in Figure 1 overlaid in red, as well as the residuals of the fit. The uncertainties presented are Poisson, and indicate the 68% error range to be somewhat analogous to the Gaussian case.

combined with a higher-temperature nonequilibrium plasma at 0.98 keV.

4.4. Derived Physical Characteristics

Using the parameters of our spectral fits we can calculate additional characteristics such as plasma density and shock velocity in order to learn more about these remnants and under what conditions they formed. Solving the Rankine–Hugoniot relations in the strong shock case with $\gamma = 5/3$ gives the post-shock temperature as a function of shock velocity, $kT = (3/16)\,\mu\, m_p\, v^2$, with the average mass per particle $\mu = 0.6$. We assume that $T_e \sim T_{\rm ion}$, as expected through Coulomb collisions in a plasma with a temperature of $\sim 10^6$ K and $n_e \sim 1\,{\rm cm}^{-3}$ (Draine 2011). If the electrons and ions are not in temperature equilibrium, then the calculated velocities signify lower bounds. The density is found using the norm parameter for each component, where norm $=[10^{-14}/(4\pi D^2)]\int n_e n_H dV$, where D is the distance to the source, in this case the SMC. The value $\int n_e n_H dV$ is the emission measure, where n_e and n_H are the electron and proton densities, and V is the volume of emitting plasma. A value of 61.3 kpc is used for D (Hilditch et al. 2005), and we assume that $n_e = 1.2 n_H$. We include a filling factor, f, which ranges from 0 to 1, to account for the fraction of the volume actually filled with X-ray-emitting plasma. We can also estimate the age of the remnant from the equilibrium shock velocities. Assuming that each remnant can be described by a Sedov solution (Spitzer 1998), the time since shock heating can be calculated as $t = (2/5)R/v$, where R is the estimated shock distance from the center. In Table 4, we detail the physical results calculated from our best-fit models.

Table 2
Best-Fit Parameters for DEM S 128

Best-Fit Model	cstat/dof	1 - (P-value)	$N_{H,SMC}$ (10^{22} cm^{-2})	kT_{vapec} (keV)	A_{Fe}	norm$_{vapec}$ (10^{-5}A)[a]
tbabs$_{gal}$ × tbvarabs$_{SMC}$ × vapec	219/200	12.4%	$0.35^{+0.14}_{-0.12}$	$0.65^{+0.03}_{-0.03}$	$0.9^{+0.2}_{-0.1}$	15^{+3}_{-2}

Note. Spectral-fitting results of DEM S 128 with extraction and background regions and Figure 2. The remnant and regions are listed in the first two columns, with the next column indicating the best-fit model. Errors shown are 1σ. Abundances are shown relative to solar, with solar values equal to 1.
[a] Normalization parameter, where $A = [10^{-14}/(4\pi D^2)] \int n_e n_H dV$, D is the distance to the SMC, and the integral is the emission measure.

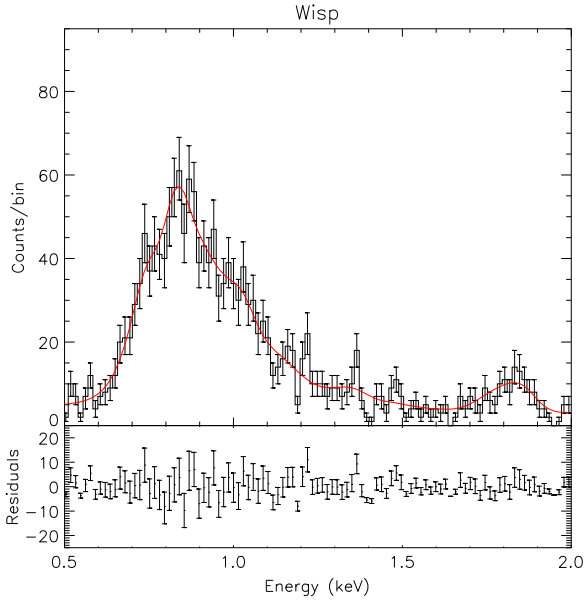

Figure 5. X-ray spectra extracted from IKT 25 from the Wisp region in Figure 1 in black with best-fit models corresponding to the best-fit model in Figure 1 overlaid in red, as well as the residuals of the fit. The uncertainties presented are Poissonian, and indicate the 68% error range to be somewhat analogous to the Gaussian case.

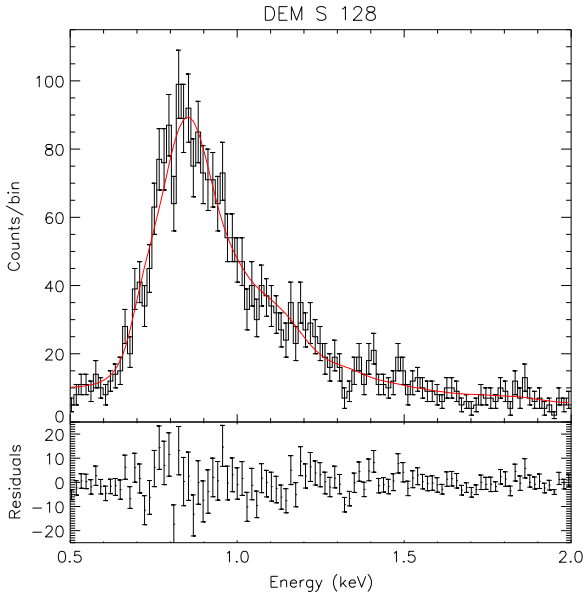

Figure 6. X-ray spectra extracted from DEM S 128 in black with best-fit models corresponding to the best-fit model overlaid in red. The uncertainties presented are Poissonian and indicate the 68% error range to be somewhat analogous to the Gaussian case.

It should be noted that in all three of these remnants, we find exotic environments that, at least in some cases, modify the plasma of the remnants asymmetrically, as detailed in the Discussion section of this paper. It is possible that none of these remnants are accurately described by a Sedov solution for this reason. In an effort to minimize this deviance from an idealized Sedov solution, we only use regions for each remnant where we have determined that the complicated environment has a minimized impact on the development of the SNR to determine its physical characteristics.

For IKT 25, the velocities derived from the fit are ~900 km s^{-1} across every region. Region C has a relatively low density, ~0.15 cm$^{-3}/f^{1/2}$, compared to Regions A, B, and D, which are >0.25 cm$^{-3}/f^{1/2}$. The Wisp has the lowest density in the remnant, with two components, both of which are <0.1 cm$^{-3}/f^{1/2}$. Therefore, even though Regions C and the Wisp exhibit the largest absorbing column densities, the X-ray-emitting plasma is relatively tenuous. DEM S 128 exhibits a relatively slow shock (~750 km s^{-1}), low density at <0.1 cm$^{-3}/f^{1/2}$, and in our sample has the largest physical X-ray size, suggesting that it is the oldest of our three remnants. IKT 5 has a low density, more consistent with DEM S 128 at ~0.1 cm$^{-3}/f^{1/2}$, even though its temperature remains relatively high.

5. DISCUSSION

5.1. IKT 25

In comparison to van der Heyden et al. (2004), we find that the temperatures across the remnant are somewhat hotter, ~1.0 keV compared to VDH04's finding of 0.6 keV. They do not examine the spatial dependence of the absorption column density and find a global absorbing column density of 4.1×10^{21} cm^{-2}, which, while consistent with our Regions A, B, and D, we find to be very low compared to our Region C and Wisp fits, whose absorbing column density is as high as 1.5×10^{22} cm^{-2}. Unlike VDH04, we do not find any evidence for enhanced Ne in the remnant. This is likely a consequence of the models in this paper being more advanced than those used in VDH04. In particular, the modeling of Fe-L shell ions from 0.8 to 1.0 keV has improved immensely in APED. The additional lines significantly increase the total line flux contribution from species in this energy range, thus decreasing the importance of the Ne lines in comparison to the newly added suite of Fe lines. When comparing to Lee et al. (2011), we find a cooler temperature than their 2.0 keV. Lee et al. (2011) also do not examine the spatial variation in the absorbing column density. Instead, they hold the column density across the remnant fixed to the value of their global fit, 9.1×10^{21} cm^{-2}. In Regions B and D, we find the absorbing column density to be as low as $\sim 3 \times 10^{21}$ cm^{-2}, with higher absorbing column density $\sim 1.5 \times 10^{22}$ cm^{-2} in Region C and

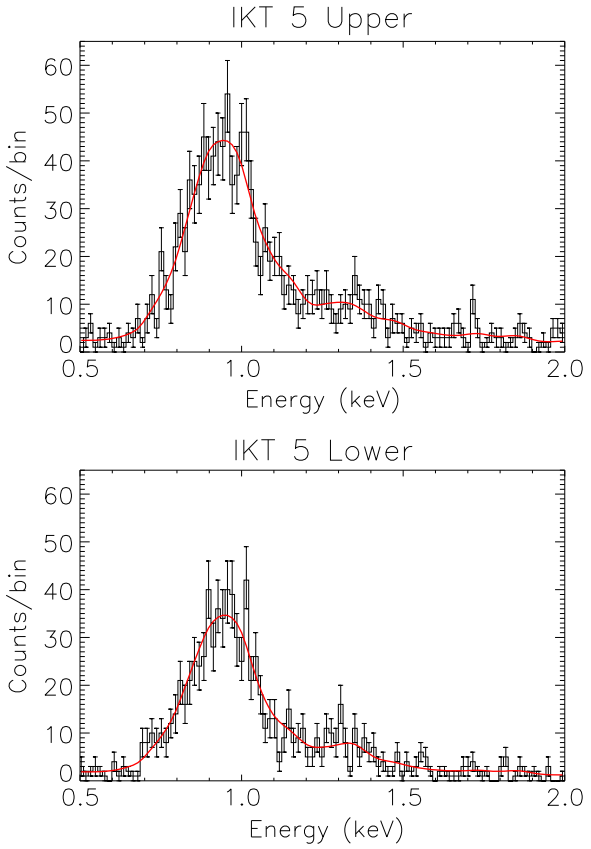

Figure 7. X-ray spectra extracted from IKT 5 in Figure 3 in black with best-fit models corresponding to the best-fit model in Figure 3 overlaid in red, by region. The uncertainties presented are Poissonian and indicate the 68% error range to be somewhat analogous to the Gaussian case.

the Wisp. In addition, our Fe overabundance is found to be more significant. Our norm-averaged Fe abundance across Regions A–D is 1.0 ± 0.1, which is 8 σ significance overabundant, whereas their norm-averaged Fe abundance across analogous regions Bar01–Bar04 is $\sim 1.08 \pm 0.32$, only 2.75 σ significance overabundant. It should be noted that a direct abundance comparison to Lee is difficult because they use the wrong abundances for the SMC. In particular, the abundances quoted in Table 1 of Lee et al. (2011) actually match the Table 1, column 8 values of Russell & Dopita (1992), which are the errors in the SMC abundances, not the abundances themselves, therefore rendering the results suspect. Using the improved statistical approach with accurate abundances and up-to-date line lists, we have more tightly constrained physical parameters and detect a more robust Fe enhancement for IKT 25, in comparison to previous studies.

Our X-ray results indicate that, with the exception of enhanced Fe, our remnant is ISM-dominated. We frame our X-ray results with data from other wavelengths to qualitatively probe how this remnant interacts with its environment. We use our IR and optical data (Figure 8) as images to compare with our X-ray and radio data for further insight into the emission of these remnants. From the radio contours of IKT 25 (Figure 9 (a)), we see evidence of a supernova (SN) blast wave traveling through material that is roughly anticoincident with the X-ray emission of the remnant. The radio emission is highly coincident with the IR emission in the northeast. Synchrotron emission in the lowest-density regions of the shock may explain the radio emission, whereas shock-heated material with subsequent cooling emission explains the IR, optical, and X-ray emission, albeit at different densities. The optical emission shows primarily cooling lines from regions in the shell with densities much higher than those in the X-ray plasma. The IR emission is roughly anticoincident with Regions A, B, and D and coincident with the Wisp region. The presence of significant IR emission suggests the existence of a local enhancement of the ISM density, which would give rise to the much higher line-of-sight (LOS) absorption column density in the Wisp region. The Wisp is also the only region in any of our remnants with enhanced Si, which is found to be >5σ. This enhancement is quite evident in the Wisp spectrum as the large bump at 1.8 keV Si XIII, especially when compared to all other spectra. This strongly suggests an enhancement of Si ejecta in this region. Its existence in the Wisp suggests that the supernova blast wave in this region is transitioning from the adiabatic phase to the radiative phase, and it contains only small pockets of gas at X-ray-emitting temperature with a low filling factor, which is consistent with a local enhancement of ISM density. The overabundance of Si in addition to Fe strongly suggests a Type Ia designation.

The bipolar morphology of IKT 25 may be due to asymmetry in the explosion mechanism of the progenitor system or modification by the environment. In either case, and especially for an asymmetric explosion, one might expect older plasma toward the center, with more recently shocked gas in Regions A and D. In this scenario we must be careful with the derived radii and velocities in Regions B and C, as they may be affected by LOS projection. In other words, much of the emitting plasma in B or C may actually be at a large radius, comparable to Regions A and D, yet just appear closer to the center in the X-ray data due to projection onto the plane of the sky. However, as seen from the X-ray spectral fit, there is a large column density associated with Region C. Inspection of the optical data reveals a band of dense material stretching across Region C, thus corresponding to the absorption seen in X-rays. In fact, the combination of X-ray, optical, IR, and radio data display a clear spherical geometry for this remnant. The band of material that is coincident in optical and radio wraps around the spherical remnant and is anticoincident with the X-ray emission, except for that in Region C. This suggests that this X-ray emission does not originate at large radii toward the observer, but must exist closer to the center of the remnant in this region. This constraint cannot be placed on Region B. For this reason, we only compare ages from the internal Region C with those found in A and D. For Regions A and D, we approximate the age using a Sedov solution, resulting in an age estimate of around 6000 yr. The ionization parameter in Region C implies a shock timescale of longer than this, at around 20,000 yr, depending on the assumed filling factor of the plasma. Therefore, the age structure of the remnant is consistent with a bipolar or directional flow of X-ray-emitting material away from the center of the remnant and toward the locations of Regions A and D. Given the large amount of IR and optically detected material located in the band surrounding the X-ray emission, it is still difficult to determine if the X-ray-emitting plasma is following a bipolar morphology due to a preferred explosion direction or pressure confinement from material in the environment.

Lee et al. (2011) have suggested that IKT 25 is produced by a so-called "prompt" Type Ia explosion mechanism. Our

Table 3
Best-Fit Parameters for IKT 5 by Extraction Region

Region	Best-Fit Model	cstat/dof	1 − (P-value)	$N_{H,\mathrm{SMC}}$ (10^{22} cm^{-2})	kT_{vapec} (keV)	A_{Fe}	$\mathrm{norm}_{\mathrm{vapec}}$ (10^{-5} A)[a]	kT_{nei} (keV)	τ_{nei} (10^{11} s cm^{-3} s)	$\mathrm{norm}_{\mathrm{nei}}$ (10^{-5} A)	F-test P-value Percentile
Northern	$\mathrm{tbabs_{gal}} \times \mathrm{tbvarabs_{SMC}} \times$ vapec	227/197	77.5%	$0.3^{+0.1}_{-0.1}$	$0.94^{+0.03}_{-0.03}$	$0.8^{+0.2}_{-0.1}$	$6.3^{+0.6}_{-0.6}$	…	…	…	…
Southern	$\mathrm{tbabs_{gal}} \times \mathrm{tbvarabs_{SMC}} \times$ (vapec + vnei)	221/194	79.1%	$0.23^{+0.08}_{-0.08}$	$0.56^{+0.03}_{-0.03}$	$2.0^{+1.3}_{-0.7}$	$0.6^{+0.8}_{-0.8}$	$1.0^{+0.1}_{-0.1}$	$1.7^{0.8}_{-0.3}$	$1.8^{1.0}_{0.2}$	0.0517

Note. Spectral-fitting results by region listed in Figure 3. The remnant and regions are listed in the first two columns, with the next column indicating the best-fit model. Errors shown are 1σ. Abundances are shown relative to solar, with solar values equal to 1.

[a] Normalization parameter, where $A = [10^{-14}/(4\pi D^2)] \int n_e n_H dV$, D is the distance to the SMC, and the integral is the emission measure.

Table 4
Physical Parameters of the SNR

Remnant	Region	$v_{shock,cie}$ (km s^{-1})	Radius (pc)	Sedov age (yr)	$n_{e,cie}$ (cm$^{-3}/f^{1/2}$)	t_{shock} (yr $\times f^{1/2}$)	$v_{shock,nei}$ (km s^{-1})	$n_{e,nei}$ (cm$^{-3}/f^{1/2}$)
IKT 25	Region A	899	14.5	6300	0.25	⋯	⋯	⋯
	Region B	885	⋯	⋯	0.45	⋯	⋯	⋯
	Region C	761	⋯	⋯	0.15	20,000	913	0.17
	Region D	936	14.3	6000	0.25	⋯	⋯	⋯
	Wisp	703	⋯	⋯	0.08	⋯	875	0.06
DEM S 128	⋯	755	21.9	11,000	0.08	⋯	⋯	⋯
IKT 5	Upper	894	13.9	6100	0.10	⋯	⋯	⋯
	Lower	691	14.1	⋯	0.05	38,000	923	0.08

Note. Physical parameters derived from the fit parameters in Tables 1–3. Shock velocity was calculated using the temperature from Tables 1–3.

Table 5
List of Point Sources in DEM S 128

J2000 Coordinates		Previously Reported Name (If Applicable)	Radio Coincident?
R.A.	Decl.		
01:05:36.3	−72° 9′ 48.″9	2XMM J010536.3-720948	No
01:05:30.9	−72° 10′ 21.″5	⋯	Yes
01:05:24.9	−72° 11′ 16.″1	⋯	Possible
01:05:9.7	−72° 11′ 48.″0	CXO J010509-721146	No
01:04:59.9	−72° 11′ 47.″7	⋯	No
01:05:50.5	−72° 12′ 37.″1	⋯	No
01:05:33.0	−72° 13′ 31.″5	⋯	No

Note. A list of the point sources within and around the supernova remnant DEM S 128. The point sources were detected using the CIAO tool *wavdetect*. Previously discovered point sources with names are given in the rightmost column.

analysis supports this idea. Indeed, IKT 25 shares a great deal with the first two SNRs to be classified in this way, DEM L238 and DEM L249 (Borkowski et al. 2006). As in the Borkowski et al. remnants, the ionization parameter is large when compared to its Sedov age, although it should be noted that both DEM L238 and DEM L249 have X-ray shells, whereas ours do not have well-defined shells in the X-ray. If we combine the results from all five regions of IKT 25, specifically the Fe abundance, the probability that they are consistent with or less than the SMC abundance of 0.2 solar is vanishingly small, equivalent to a $\sim 10\sigma$ significance. The global norm-averaged overabundance of greater than 8σ of Fe for IKT 25 and the presence of enhanced Si in the Wisp also argues strongly for the Type Ia designation.

5.2. DEM S 128

Aside from the absorbing column density, we find different physical parameters for DEM S 128 than those determined in VDH04. As with IKT 25, we find a significantly enhanced Fe abundance (7σ). All other elements are consistent with SMC ISM values, which contradicts the overabundance of Mg and Si reported in VDH03. An overabundance of these species should be seen as clear line signatures at 1.3 and 1.8 keV, respectively, which is not observed in the spectrum (Figure 6). Our enhanced Fe abundance and lack of Mg argue more strongly for a Type Ia designation.

As in the case of IKT 25, the X-ray spectrum of DEM S 128 suggests it is ISM-dominated, aside from Fe. In order to form a qualitative understanding of the interaction of DEM S 128 with its surroundings, we turn to other wavelengths for additional information. When examining IR data for DEM S 128, we see that there is very little in the way of extended sources. We observe an absence of dense shell emission from the SN blast wave, in stark contrast to IKT 25. In fact, we see no IR emission that is obviously associated with this SNR whatsoever. This may suggest a highly rarefied medium, which is consistent with the low density derived from the X-ray emission and Type Ia designation. However, it should be noted that the presence of plasma in CIE, as suggested by our fits, is inconsistent with this picture.

However, there are a number of discrete radio sources that are coincident with X-ray emission. Our point-source analysis of the X-ray image revealed seven point-source detections. These sources are diagrammed in the center panel of Figure 10, which also overlays the radio data as white contours. The positions of these objects are given in Table 5. Of the seven, two were previously identified in X-ray point-source catalogs, 2XMM J010536.3-720948 and CXO J010509-721146. Most of these X-ray point sources have no coincident radio emission greater than five times the local background flux. Intriguingly, one X-ray point source, labeled Source 2, does exhibit strong coincident radio emission. This object is only slightly extended when compared to the beam size of this midresolution radio image. Unfortunately, there are only a total of 69 X-ray source counts, which is not enough to spectrally analyze this point source to confirm its nonthermal nature. However, the off-axis nature of the X-ray observation leads to a large PSF and questionable discreteness of these sources. Also, high-resolution radio data over multiple frequencies would determine the spectral index, which should be flat, to be consistent with a PWN. On-axis, longer-duration *Chandra* observations combined with higher-resolution radio data could confirm that this source is indeed a PWN, contradicting the Type Ia designation. Further complicating the classification of DEM S 128 is its close positional coincidence with the star-

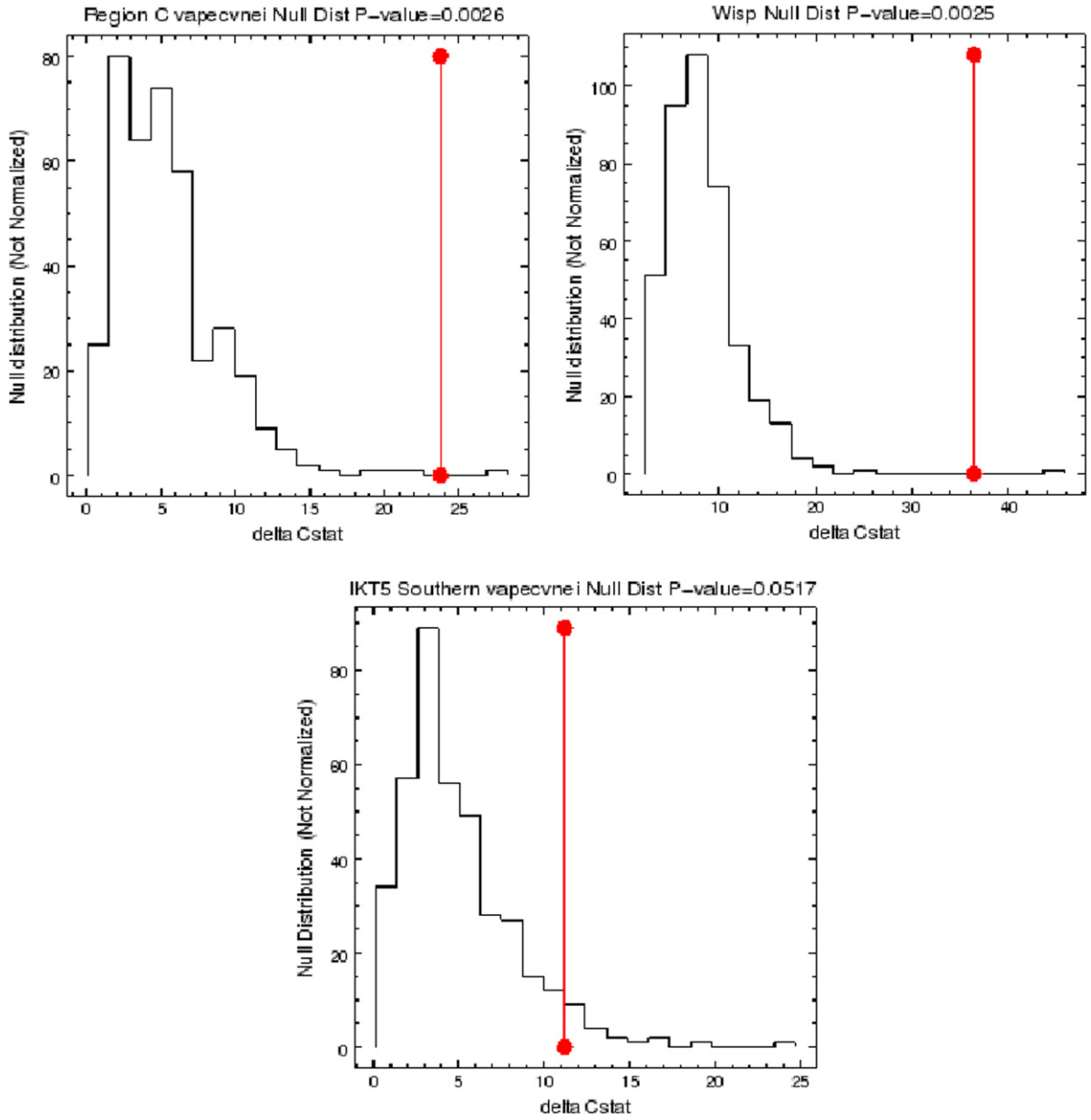

Figure 8. Results of the parametric bootstrapping method we replace the F-test with, as described in Section 3. All of these were constructed using 400 simulated spectra produced by adding a Poisson noise component to each fit's respective best-fit one temperature model. (a) The results for the parametric bootstrapping of IKT 25 Region C (see Table 1 for final fit parameters). (b) The results for the parametric bootstrapping of the IKT 25 Wisp region (see Table 1 for final fit parameters). (c) The results for the parametric bootstrapping of the IKT 5 southern region (see Table 3 for final fit parameters).

forming region (SFR), DEM S 124. If DEM S 128 is a member of this SFR, it seems likely that it is a CC remnant. This association would also explain the rarefied medium as being due to strong stellar winds.

The optical emission in of DEM S 128 is presented at the bottom of Figure 9. There is an optical circular shell filled with emission, but the center of this shell is some 45 pc spatially separated to the north of the X-ray remnant with no overlap. This optical feature is closer to the position of the original source, labeled DEM S 128 by Davies et al. (1976), but the X-ray remnant is more consistent with the position of the source reported by Inoue et al. (1983). An arc of optical emission appears to surround the X-rays, suggesting that the hotter gas is contained within this feature, but the high level of field confusion evident in the optical may make this association purely coincidental. If the radio and X-ray bright source is a PWN, it strongly indicates that DEM S 128 is of CC origin. This suggests that DEM S 128 is not a Type Ia SNR at all, but rather is the product of a CC explosion that produced the overabundance of Fe observed in the X-ray spectrum.

5.3. IKT 5

The X-ray results in this remnant are perhaps the most perplexing of the three remnants. The northern region has an Fe overabundance at 0.8 solar, which is significantly above the SMC abundance by about 4σ, whereas the southern region has an Fe abundance of twice solar, but the error bars on this particular region are large enough to be consistent with SMC ISM. As in Region C and the Wisp region of IKT 25, the southern region's CIE fit is relatively cool at 0.56 keV, whereas

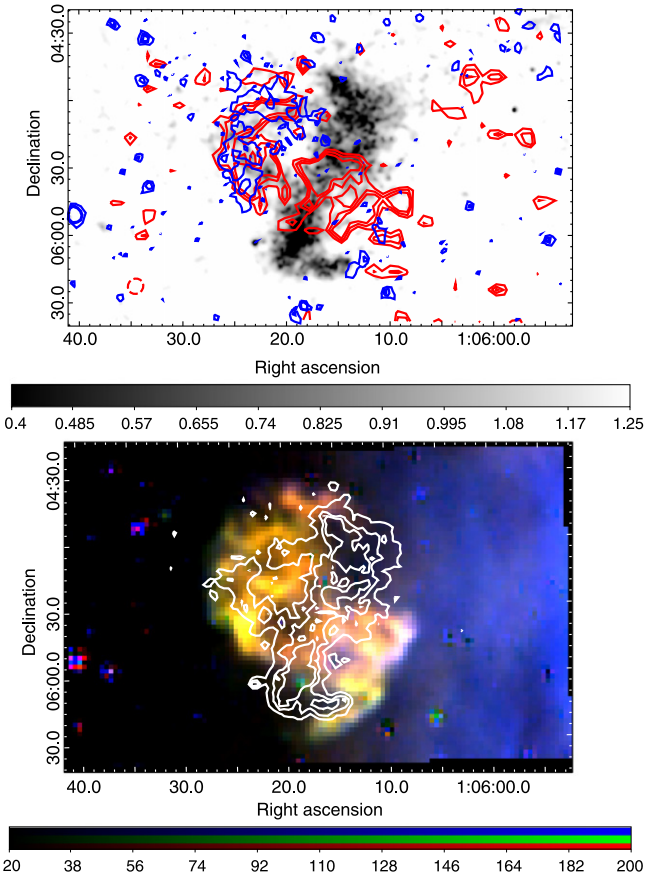

Figure 9. IKT 25 in other wavelengths. IKT 25 X-ray data in linear grayscale; the blue overlaid contours are 8 μm IRAC *Spitzer* data, and the red overlaid contours are ATCA 20 cm flux (top). The 8 μm IRAC contours are in units of 0.8, 1.0, and 1.2 MJy/Sr ($\sim 4\sigma$, 5σ, and 6σ), whereas the radio contours are in units of 90, 120, and 150 μJy /beam ($\sim 3\sigma$, 4σ, and 5σ). Optical MCELS RGB image of IKT 25, with ACIS contours overlaid (bottom). The red, green, and blue are continuum-subtracted [S II], Hα, and [O III], respectively.

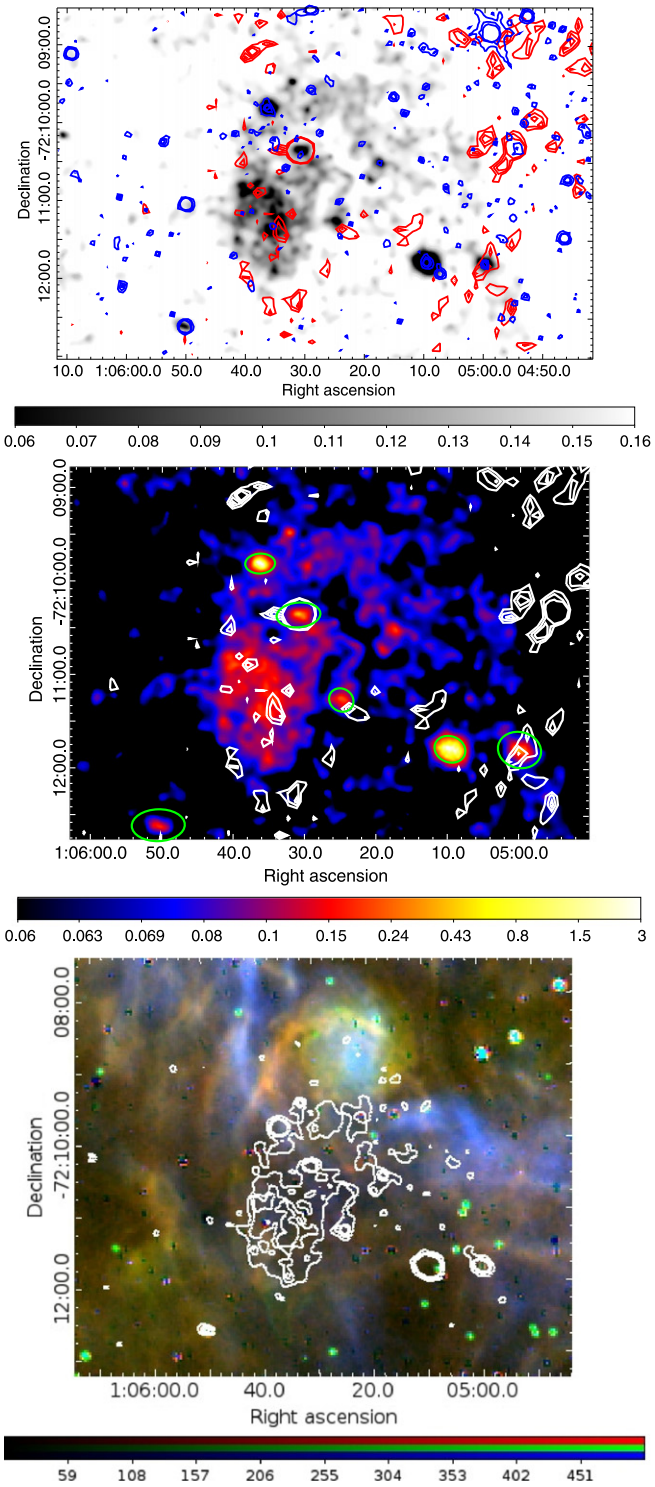

Figure 10. DEM S 128 X-ray data in linear grayscale; the blue overlaid contours are 8 μm IRAC *Spitzer* data, and the red overlaid contours are ATCA 20 cm flux (top). The 8 μm IRAC contours are in units of 0.8, 1.0, and 1.2 MJy/Sr ($\sim 4\sigma$, 5σ, and 6σ), whereas the radio contours are in units of 90, 120, and 150 μJy /beam ($\sim 3\sigma$, 4σ, and 5σ). DEM S 128 in the ACIS 0.5–2.0 keV waveband is in color, and the 20 cm radio is in white contours in units of 90, 120, and 150 μJy (middle). The green regions in the X-ray image are detected point sources, with labels indicating previously detected point sources. Optical MCELS RGB image of DEM S 128, and with ACIS contours overlaid (bottom). The red, green, and blue are continuum-subtracted [S II], Hα, and [O III], respectively.

the NEI component is at 1.0 keV. The values of the absorbing column density across IKT 5 found by VDH04 are consistent with our results. VDH04 find a very high ionization timescale, and while this is consistent with our Upper Region, which is in CIE, it is inconsistent with our fit result in the Lower Region, which has a component out of ionization equilibrium with a timescale that is smaller than the lower limit listed in VDH04. As with IKT 25, VDH04 find enhanced Ne, which we do not require in order for a good fit. Again, this is mostly due to the overlap of the Fe-L shell and the Ne-K shell in energy. The X-ray results on their own, as with IKT 25 and DEM S 128, suggest a Type Ia origin.

To explore this classification further, we perform a point-source analysis on IKT 5, given previous suggestions of a point source (van der Heyden et al. 2004; Laycock et al. 2010). We detect a source within the remnant that is coincident with the CXOU J004824-731918 source reported in Laycock et al. (2010). Figure 11 (upper right) shows the 3σ *wavdetect* psf extent as a green ellipse with high-energy, 2.0–8.0 keV emission in white contours. The peak of the high-energy emission is coincident with the location of the point source, suggesting that this source is not simply a bright knot of emission from the SNR. Given the Laycock et al. (2010) conclusion that the point source is likely not an XRB, the possibility exists that this source is a PWN or compact central

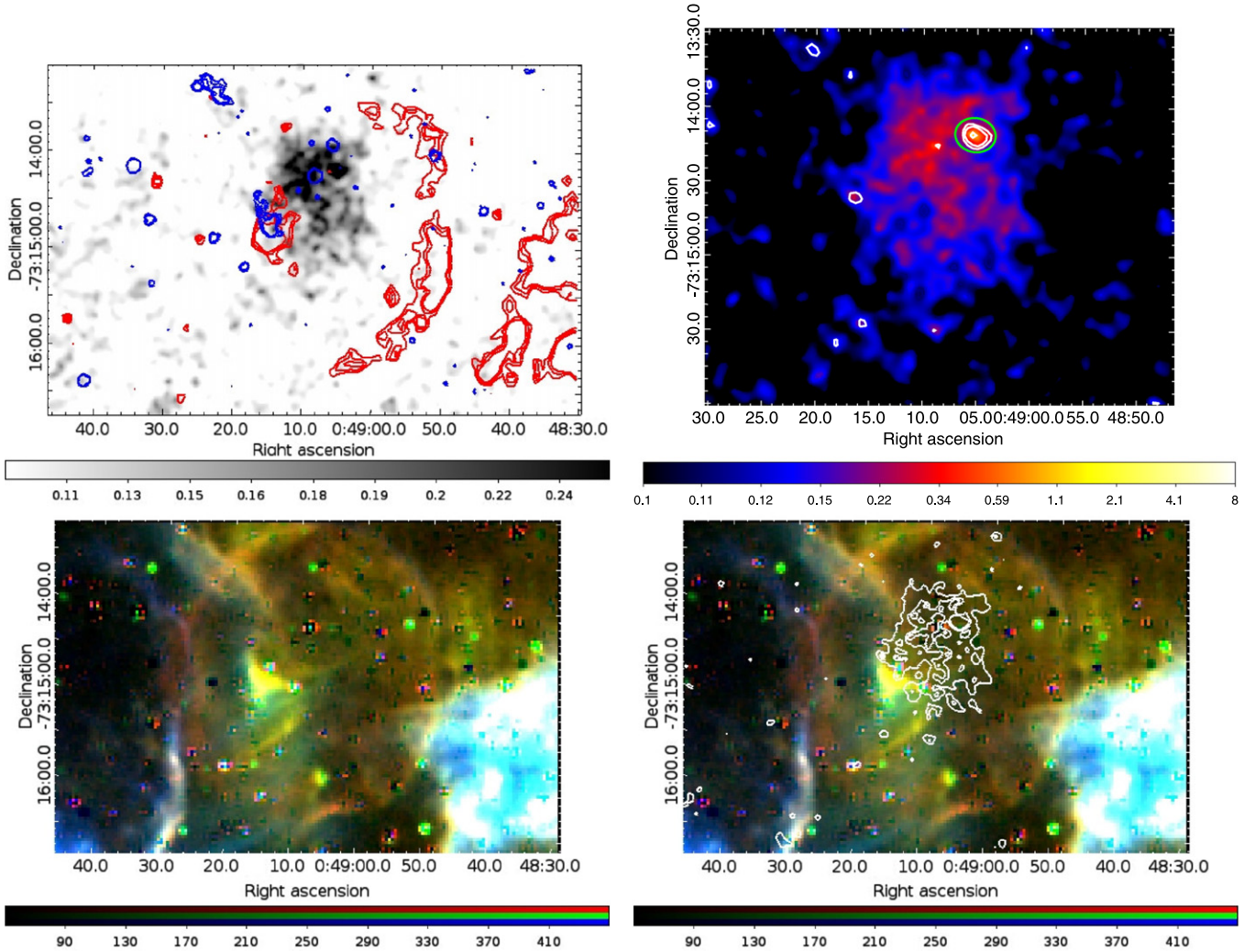

Figure 11. IKT 5 data in linear grayscale; the blue overlaid contours are 8 μm IRAC *Spitzer* data, and the red overlaid contours are ATCA 20 cm flux (upper left). The 8 μm IRAC contours are in units of 0.8, 1.0, and 1.2 MJy/Sr (~4σ, 5σ, and 6σ), whereas the radio contours are in units of 90, 120, and 150 μJy /beam (~3σ, 4σ, and 5σ). The X-ray images are detected point sources in white and green contours in units of 0.12, 0.15, and 0.3 counts/pixel of the ACIS data from 2.0–8.0 keV (upper right).IKT 5 in the MCELS optical band. The red, green ,and blue are continuum-subtracted [S II], Hα, and [O III], respectively (lower left). Optical MCELS RGB image of IKT 5, with ACIS contours overlaid (lower right).

object. Spectra extracted from just the point-source region were too low significance to perform meaningful spectral fits to verify this possibility. Longer, on-axis *Chandra* observations are necessary in order to further constrain the nature of this point source, yet the current characteristics challenge a typical Type Ia designation.

As in the IKT 25 and DEM S 128 cases, only Fe was overabundant, indicating that this is a highly ISM-dominated remnant. Figure 11 (upper left) shows that to the southeast of the X-ray remnant there is a small, diffuse knot of infrared emission that is roughly anticoincident with the X-ray emission in the southern region. We find from the shorter-wavelength IR images (not presented here) that this knot is actually unresolved point-source emission from a star cluster in the area and is likely not associated with the remnant. Also evident is an IR source in the middle of the remnant, coincident with a known red supergiant 2MASS J00490818-7314155 (Massey & Olsen 2003). It is unclear to what extent any of the IR emission in this field is associated with IKT 5.

The radio observation for IKT 5 is also shown in the upper left panel of Figure 10. The hard X-ray point source found in our analysis is not detected in the radio, making a PWN within the remnant questionable. However, the telescope array was optimized for diffuse emission. An observation using an array configuration optimized for spatial resolution is necessary to determine the strength of the point-source radio emission. In addition, further to the west of the remnant there is a half-shell in the radio consistent with shocked gas. This half-shell appears to have its center positionally consistent with the X-ray remnant. The optical emission completes this western radio shell in Hα and [S II] (Figure 10, bottom left). The optical image also reveals a secondary, inner optical bubble that appears just exterior to the X-ray emission. The inner bubble of this "double bubble" structure could be the SN shock front. This volume would then be filled with hot, X-ray-emitting gas. The outer, larger bubble is clearly also shocked gas, but is far outside the remnant. Such a shock could be due to the progenitor system. A massive star progenitor could have blown a cavity with its strong stellar wind. The ~50 pc physical size of this bubble is consistent with typical wind speeds (1000 km s^{-1}) and lifetimes (10^5–10^6 yr) of massive stars. The inner SN blast wave is in the process of catching up with

the outer bubble, which has a head start on the order of the lifetime of the massive star.

Our analysis suggests that IKT 5 may not be of Type Ia origin. The detection of the possible X-ray point source with surrounding high-energy emission is indicative of a leftover compact object, thus being consistent with the picture of a massive progenitor, as are the combined optical and radio data. However, the large Fe abundance argues against at least a typical CC SNR. In addition, the current lack of coincident radio emission argues that the potential compact object is unlikely to be a PWN, yet higher-resolution data are needed for verification. As with DEM S 128, the X-ray observation of IKT 5 was well off-axis, thus leading to a poor PSF and questionable point-source detection. Given the environmental conditions present in the multiwavelength analysis, there is stronger evidence of a CC origin for IKT 5. However, we cannot rule out the possibility that IKT 5 is another member of the same class SNR as IKT 25 and DEM s 128. It is important to acquire higher-quality, on-axis, longer-exposure X-ray data to ensure the nature of this point source and its high-energy emission, as well as high-resolution radio data. This would clarify the classification of this SNR and identify the central compact object.

6. SUMMARY

By applying the most modern X-ray plasma models available, in addition to using the Cash statistic, we have analyzed these remnants in the low-counts regime. The best-fit spectral models of these three SNRs indicate that they are both moderately aged and strongly ISM-dominated. However, despite the information lost in their advanced age, there is significant emission indicative of Fe overabundance in all the remnants we analyzed. The extent of these enhancements is too much to be due to the fluctuation of the ISM (Russell & Dopita 1992). This Fe overabundance is the biggest piece of evidence that points toward these three remnants being Type Ia SNRs. However, it is important to note that as the plasma models utilized in X-ray spectral fitting develop, in particular with the release of APEC version 3.0, there will be more support for Fe lines in the Fe-L shell, and the true abundance of Fe may be found to be somewhat less than reported in this paper. While the Fe content of each remnant argues for a Type Ia classification, these objects also display characteristics of CC remnants, such as dense environments, local star-forming regions, and possible progenitor point sources. Although we did not require varying oxygen abundance in the fit, when we allow the oxygen to vary, these remnants yield a lower abundance of oxygen than is usually produced from CC SNe, with [O/Fe] $\lesssim$0.5. Such a ratio has been achieved in nucleosynthesis models of low-metallicity progenitors with a mass of $\lesssim$15 $M_{\odot}$, which might be found in the SMC.

Lopez et al. (2011) make the case for ejecta-dominated Type Ia SNRs being more symmetric than CC SNRs, which was in conflict with IKT 25, DEM S 128, and IKT 5's tentative Type Ia classification by VDH04, especially compared to highly symmetric CC remnants in the SMC. Our analysis has shown that the apparent contradiction of these remnants evident in VDH04 with the study of Lopez et al. (2011) is only skin-deep. With the current X-ray data, it is uncertain what types of SN explosion were the progenitors of IKT 25, IKT 5, and DEM S 128. While we confirm that there is a significant Fe overabundance through X-ray spectroscopy, each has oddities that preclude their being a "classical" Type Ia SNR. In addition, these remnants show a high degree of ISM domination in their X-ray spectra, indicating a high degree of morphological alteration by the environment. If these remnants are Type Ia SNRs at all, they likely all originated from prompt Type Ia progenitor systems, which are fundamentally different than those studied by Lopez et al. (2011), so that even morphological comparison between these three remnants and their oxygen-rich CC cousins in the SMC may not be appropriate.

This research has made use of data obtained from the *Chandra* Data Archive and the *Chandra* Source Catalog and software provided by the *Chandra* X-ray Center (CXC) in the application packages CIAO, ChIPS, and Sherpa. The infrared data were obtained from the *Spitzer* Heritage Archive.[3] We obtained the optical data from the Magellanic Cloud Emission Line Survey.[4]

REFERENCES

Badenes, C., Borkowski, K. J., Hughes, J. P., Hwang, U., & Bravo, E. 2006, ApJ, 645, 1373
Borkowski, K. J., Hendrick, S. P., & Reynolds, S. P. 2006, ApJ, 652, 1259
Cash, W. 1979, ApJ, 228, 939
Davies, R. D., Elliott, K. H., & Meaburn, J. 1976, MmRAS, 81, 89
Dickey, J. M., & Lockman, F. J. 1990, ARA&A, 28, 215
Draine, B. T. 2011, in Physics of the Interstellar and Intergalactic Medium (Princeton, NJ: Princeton Univ. Press)
Filipović, M. D., Haberl, F., Pietsch, W., & Morgan, D. H. 2000, A&A, 353, 129
Filipović, M. D., Payne, J. L., Reid, W., et al. 2005, MNRAS, 364, 217
Flanagan, K. A., Canizares, C. R., Dewey, D., et al. 2004, ApJ, 605, 230
Foster, A. R., Ji, L., Smith, R. K., & Brickhouse, N. S. 2012, ApJ, 756, 128
Freeman, P., Doe, S., & Siemiginowska, A. 2001, Proc. SPIE, 4477, 76
Fruscione, A., McDowell, J. C., Allen, G. E., et al. 2006, Proc. SPIE, 6270, 62701V
Hilditch, R. W., Howarth, I. D., & Harries, T. J. 2005, MNRAS, 357, 304
Hughes, J. P., & Smith, R. C. 1994, AJ, 107, 1363
Inoue, H., Koyama, K., & Tanaka, Y. 1983, in IAU Symp. 101, Supernova Remnants and their X-ray Emission, ed. J. Danziger, & P. Gorenstein (Dordrecht: Reidel), 535
Laycock, S., Zezas, A., Hong, J., Drake, J. J., & Antoniou, V. 2010, ApJ, 716, 1217
Lee, J.-J., Park, S., Hughes, J. P., Slane, P. O., & Burrows, D. N. 2011, ApJL, 731, L8
Lopez, L. A., Ramirez-Ruiz, E., Huppenkothen, D., Badenes, C., & Pooley, D. A. 2011, ApJ, 732, 114
Massey, P., & Olsen, K. A. G. 2003, AJ, 126, 2867
Payne, J. L., White, G. L., Filipović, M. D., & Pannuti, T. G. 2007, MNRAS, 376, 1793
Protassov, R., van Dyk, D. A., Connors, A., Kashyap, V. L., & Siemiginowska, A. 2002, ApJ, 571, 545
Russell, S. C., & Dopita, M. A. 1992, ApJ, 384, 508
Sault, R. J., Teuben, P. J., & Wright, M. C. H. 1995, in ASP Conf. Ser. 77, Astronomical Data Analysis Software and Systems IV, ed. R. A. Shaw, H. E. Payne, & J. J. E. Hayes (San Francisco, CA: ASP), 433
Spitzer, L. 1998, Physical Processes in the Interstellar Medium (Weinheim: Wiley-VCH)
van der Heyden, K. J., Bleeker, J. A. M., & Kaastra, J. S. 2004, A&A, 421, 1031
Verner, D. A., Ferland, G. J., Korista, K. T., & Yakovlev, D. G. 1996, ApJ, 465, 487
Wilms, J., Allen, A., & McCray, R. 2000, ApJ, 542, 914

[3] The *Spitzer* Heritage Archive can be found at http://sha.ipac.caltech.edu/applications/Spitzer/SHA/
[4] http://astro.wsu.edu/worthey/html/mcsurvey.html